# Spin-Torque-Based Quantum Fourier Transform

Anant Kulkarni and Brajesh Kumar Kaushik

Department of Electronics and Communication Engineering, Indian Institute of Technology-Roorkee, Roorkee 247667, India

**Quantum computing (QC) provides an efficient platform to solve complex problems such as number factoring and searching. The quantum Fourier transform (QFT) is an integral part of quantum algorithms for integer number factoring, phase estimation, discrete algorithms, interchange of position and momentum states, quantum key distribution protocol, multiparty quantum telecommunication, and quantum arithmetic. The theoretical and experimental implementations of QFT on various platforms have been proposed by researchers. Spin-torque-based qubit(s) manipulation is one of the encouraging solid-state device technologies. However, to date, QFT is not realized by spin-torque-based QC architecture. In this article, the spin-torque-based architecture has been modeled with the help of optimized decomposition of quantum circuits for the QFT. Moreover, an optimal-depth Clifford + T gates set-based quantum circuit is utilized to implement the QFT. The performance analysis in terms of fidelity (>99%), magnitude, and phase difference of respective density matrices for different forms of three-qubit QFT provides a novel way of its physical realization to address the complex problems.**

*Index Terms*— **Decomposition, density matrix, quantum computing (QC), quantum Fourier transform (QFT), spin Hall effect (SHE), spin torque, spintronics.**

## I. Introduction

COMPLEX computing problems can be solved efficiently by quantum computing (QC) in comparison with classical computing [1]. Quantum computers are able to efficiently solve problems such as unorganized data searching [2], number factoring [3], counting solution problem [4], hidden subgroup problem [5], and security of cryptographic systems [6]. Moreover, quantum computers can perform operations in polynomial time compared to classical computers. However, the most critical issue with the QC is its physical realization. At present, the physical realization of QC is possible with the help of a classical computer and up to some extent by a quantum computer. However, the technologies for the physical realization of the quantum computer are not developed enough to deal with complex computing applications; therefore, most of the QC-based problems are solved on classical computers. To get rid of these obstacles, researchers are actively involved in the implementation of large scale QC. QC developed rapidly when [7] through his algorithm showed that QC-based integer number factoring could be performed in polynomial time. The integral component of the Shor's algorithm is quantum Fourier transform (QFT). From the computing point of view, QFT is one of the most imperative computational problems and finds its application in discrete algorithms [3], phase estimation [8], interchange of position and momentum states [8], quantum key distribution protocol [9], multiparty quantum telecommunication [10], and quantum arithmetic [11].

QFT is physically realized with the help of bulk resonance, atomic, and solid-state implementations [12]. QFT based on solid-state technologies shows enormous prospects to realize the QC at nanoscale. Recently, a spin-torque-based architecture has emerged as one of the novel technologies to realize the single-qubit rotation and two-qubit entanglement [13]. However, the number of elementary operations required to realize the QC with this architecture is an issue due to the quantum circuit decomposition required for the elementary level. Therefore, in this article, the optimal decomposition of the QFT and its realization with the generalized spin-torque-based QC architecture is presented. For every quantum operation, the iterant spins are required to be generated and injected into the channel. There are several ways to generate spin-polarized electrons. One of them is through the spin-transfer and spin-orbit torque-based mechanisms [14], [15].

The article consists of eight sections including the introduction. Section II presents the mathematical treatment for the $n$-qubit QFT. The decomposition of the phase-controlled gates used in quantum circuits for $n$-qubit QFT is elaborated in Section III. In Section IV, decomposed quantum circuits are reduced and then optimized. The realization of three-qubit QFT on spin-torque-based $n$-qubit architecture is presented in Section V. The performance of the three-qubit QFT in terms of output state density matrix, magnitude/phase difference, and fidelity comparison for the different forms of three-qubit QFT is explained in Section VI. The Clifford + T gate set-based implementation of the QFT is presented in Section VII. Finally, conclusions are drawn in Section VIII.

## II. Multi-Qubit Quantum Fourier Transform

The discrete Fourier transform (DFT) finds its applications in digital signal processing for the conversion of time-domain signals into the frequency domain. The DFT of an $n$-bit input is given as

$$\mathrm{DFT}(k) = \sum_{n=0}^{N-1} x(n) \times e^{\frac{-j2\pi nk}{N}} \tag{1}$$

where $N$ is the number of samples. However, for the complex signals, in comparison with QFT, DFT requires comparatively

Manuscript received March 1, 2019; revised May 26, 2019; accepted July 17, 2019. Date of publication August 27, 2019; date of current version October 17, 2019. Corresponding author: B. K. Kaushik (e-mail: bkk23fec@iitr.ac.in).

Color versions of one or more of the figures in this article are available online at http://ieeexplore.ieee.org.

Digital Object Identifier 10.1109/TMAG.2019.2931278

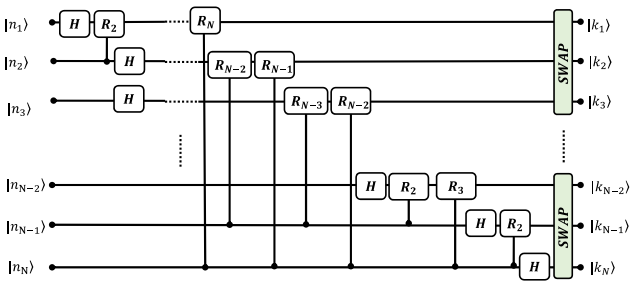


Fig. 1. $N$-qubit QFT.

large time for the time domain to frequency-domain conversion [16]. Therefore, QFT can be utilized for the time domain to the frequency-domain conversion. The QFT on $n$-qubit states is expressed as

$$\mathrm{QFT}_N|k\rangle = \frac{1}{\sqrt{N}} \sum_{n=0}^{2^{N-1}} e^{\frac{j2\pi nk}{N}} |n\rangle \tag{2}$$

where $|n\rangle$ and $|k\rangle$ are the input and output states of the qubits, respectively, and $N$ is the number of qubits. (2) is further decomposed as

$$\mathrm{QFT}_N|k\rangle = \frac{1}{2^{\frac{N}{2}}} \sum_{n=0}^{1} \cdots \sum_{n_N=0}^{1} e^{\frac{j2\pi k(\sum_{l=1}^{N} n_l 2^{-l})}{2^N}} |n_l.....n_N\rangle \tag{3}$$

$$\mathrm{QFT}_N|k\rangle = \frac{1}{2^{\frac{N}{2}}} \sum_{n=0}^{1} \cdots \sum_{n_N=0}^{1} \bigotimes_{l=1}^{N} e^{\frac{j2\pi nkl2^{-l}}{2^N}} |n_l\rangle \tag{4}$$

$$\mathrm{QFT}_N|k\rangle = \frac{1}{2^{\frac{N}{2}}} \bigotimes_{l=1}^{N} \left( \sum_{n_l=0}^{1} e^{j2\pi nkl2^{-l}} |n_l\rangle \right) \tag{5}$$

$$\mathrm{QFT}_N|k\rangle = \frac{1}{2^{\frac{N}{2}}} \bigotimes_{l=1}^{N} \left(|0\rangle + e^{j2\pi k 2^{-l}}|1\rangle\right). \tag{6}$$

Based on (6), QFT is constructed for $n$-qubits (Fig. 1). The quantum circuit for QFT consists of Hadamard and controlled phase shift gates [16].

$H$ and $R$ represent the Hadamard and controlled phase gate, respectively. A SWAP gate is utilized at the end between successive odd- and even-numbered qubits, respectively (1 and 3, 2 and 4). A four-qubit QFT for the unitary operation is represented as

$$\mathrm{QFT}_4 = \begin{bmatrix} 1 & 1 & 1 & 1 \\ 1 & i & -1 & -i \\ 1 & -1 & 1 & -1 \\ 1 & -i & -1 & i \end{bmatrix}. \tag{7}$$

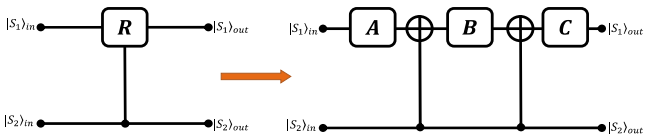


Fig. 2. Controlled unitary gate.

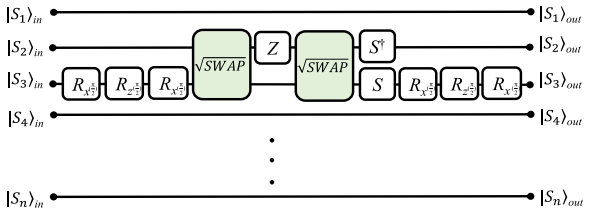


Fig. 3. Conventional CNOT gate decomposition

## III. Decomposition of Phase-Controlled Gate for Multi-Qubit QFT

A phase-controlled gate performs an unitary operation $U$ [14] that is represented as

$$U = A \cdot X \cdot B \cdot X \cdot C. \tag{8}$$

Therefore, the decomposition of the phase-controlled gate [16] for (8) is shown in Fig. 2.

The expressions for $A$, $B$, $C$, and $X$ are given in the following equations:

$$A = \begin{bmatrix} e^{-i\left(\frac{\delta-\beta}{4}\right)} & 0 \\ 0 & e^{i\left(\frac{\delta-\beta}{4}\right)} \end{bmatrix} \tag{9}$$

$$B = \begin{bmatrix} \cos(\gamma/4)e^{i\left(\frac{\beta+\delta}{4}\right)} & -\sin(\gamma/4)e^{-i\left(\frac{\beta+\delta}{4}\right)} \\ \sin(\gamma/4)e^{i\left(\frac{\beta+\delta}{4}\right)} & \cos(\gamma/4)e^{-i\left(\frac{\beta+\delta}{4}\right)} \end{bmatrix} \tag{10}$$

$$C = \begin{bmatrix} \cos(\gamma/4)e^{-i\frac{\beta}{2}} & -\sin(\gamma/4)e^{-i\frac{\beta}{2}} \\ \sin(\gamma/4)e^{i\frac{\beta}{2}} & \cos(\gamma/4)e^{i\frac{\beta}{2}} \end{bmatrix} \tag{11}$$

$$X = \begin{bmatrix} 0 & 1 \\ 1 & 0 \end{bmatrix} \tag{12}$$

where $\delta$, $\beta$, and $\gamma$ are the phase angles such that the unitary operation $U$ for the phase rotation is performed. Matrix $X$ represents the CNOT gate operation. Therefore, (8) is modified to (13), as shown at the bottom of this page.

The controlled rotations in QFT are of the unitary form as

$$R_K = \begin{bmatrix} 1 & 0 \\ 0 & e^{\frac{i2\pi}{2^K}} \end{bmatrix}. \tag{14}$$

$$U = \begin{bmatrix} \sin^2\left(\frac{\gamma}{4}\right)e^{i\beta} + \cos^2\left(\frac{\gamma}{4}\right)e^{-i\left(\frac{\beta+\delta}{2}\right)} & \sin\left(\frac{\gamma}{4}\right)\cos\left(\frac{\gamma}{4}\right)\left(e^{i\beta} - e^{-i\left(\frac{\beta+\delta}{2}\right)}\right) \\ \sin\left(\frac{\gamma}{4}\right)\cos\left(\frac{\gamma}{4}\right)\left(e^{i\left(\frac{\beta+\delta}{2}\right)} - e^{-i\beta}\right) & \sin^2\left(\frac{\gamma}{4}\right)e^{-i\beta} + \cos^2\left(\frac{\gamma}{4}\right)e^{i\left(\frac{\beta+\delta}{2}\right)} \end{bmatrix} \tag{13}$$

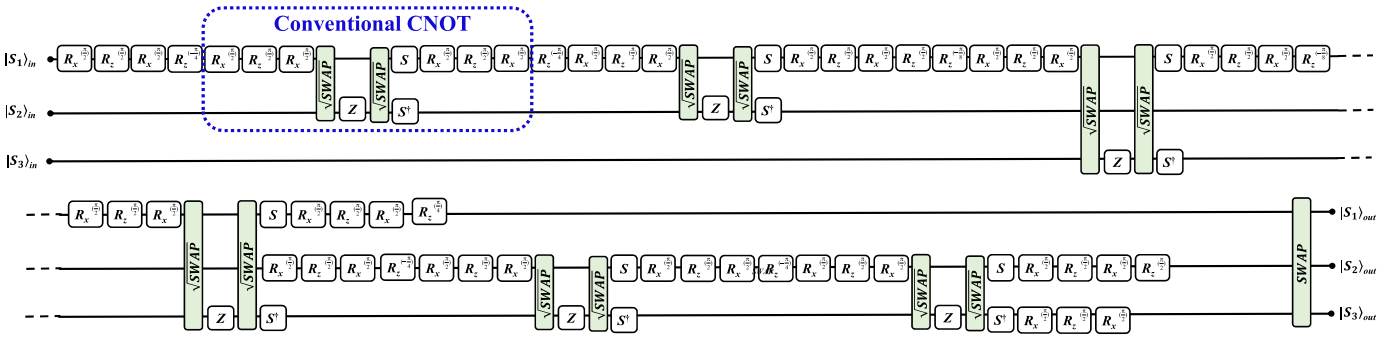


Fig. 4. Conventional decomposition of three-qubit QFT.

TABLE I
NUMBER OF ELEMENTARY OPERATIONS

| QFT size | Conventional decomposition | Reduced decomposition | Optimal decomposition |
|---|---|---|---|
| 3 | 84 | 55 | 54 |
| 4 | 162 | 106 | 103 |
| 5 | 265 | 175 | 169 |
| 6 | 393 | 261 | 251 |
| 7 | 546 | 364 | 347 |
| 8 | 724 | 484 | 463 |
| 9 | 927 | 621 | 593 |
| 10 | 1155 | 775 | 739 |

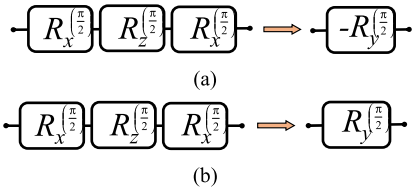


Fig. 5. (a) Initial Hadamard. (b) Final Hadamard operations for CNOT gate reduction.

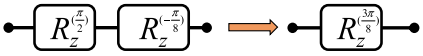

Fig. 6. Optimization technique for three-qubit QFT.

For the controlled rotations, (13) is required to be equivalent to (14) which is possible when $\delta = -3\beta$ (for smaller values of $\beta$).

After necessary modifications, (13) becomes

$$U = \begin{bmatrix} e^{i\beta} & 0 \\ 0 & e^{-i\beta} \end{bmatrix} = \begin{bmatrix} e^{-i3\delta} & 0 \\ 0 & e^{i3\delta} \end{bmatrix}. \tag{15}$$

## IV. REDUCTION/OPTIMIZATION OF QFT

The spin-torque-based architecture needs further decomposition of the Hadamard, controlled phase, and CNOT into the single-qubit rotations and two-qubit entanglements. A conventional CNOT is decomposed into 11 elementary operations in sequence [13] (Fig. 3).

The $R_x$, $R_z$, and $\sqrt{SWAP}$ are single-qubit rotation about the $x$-axis, single-qubit rotation about the $z$-axis, and two-qubit entanglement, respectively. The matrix representation of the $\sqrt{\text{SWAP}}$ is given in (16). With the help of decomposed CNOTs, $H$ gates, and single-qubit rotations, conventional decomposition of three-qubit QFT is achieved. For a ten-qubit QFT, the number of operations required is 739 (Table I). The elementary decomposition of the three-qubit QFT is shown in Fig. 4

$$\sqrt{\text{SWAP}} = \begin{bmatrix} 1 & 0 & 0 & 0 \\ 0 & \frac{1}{2}(1+i) & \frac{1}{2}(1-i) & 0 \\ 0 & \frac{1}{2}(1-i) & \frac{1}{2}(1+i) & 0 \\ 0 & 0 & 0 & 1 \end{bmatrix}. \tag{16}$$

From the spin-torque-based architecture point of view, the number of elementary operations required to realize the conventional decomposition of the QFT must be reduced with the help of techniques presented in [17] and [18]. The reduction and optimization techniques are given in Figs. 5 and 6, respectively [19].

QFT is optimized further by reducing the number of single-qubit operations about the same axis at the interface of two quantum gates (Fig. 6). The optimization of QFTs with more number of qubits can be performed with the same methodology. There is a considerable reduction in the number of elementary operations due to optimization (Table I). The number of elementary operations required to realize the QFT for their conventional, reduced, and optimized forms up to ten qubits is given in this article.

The reduction in the number of elementary operations helps in minimizing the number of switching activities needed for the spin generation and injection, preserves the spin-qubit coherence, and reduces overall switching power dissipation. For the spin-torque-based QC architecture, the number of operations with the help of quantum gate library $\{R_y, R_z, \sqrt{SWAP}\}$ is reduced. $R_y$ is the qubit rotation about the $y$-axis. The reduced/optimized decomposition of the three-qubit QFT is shown in Fig. 7.

## V. SPIN-TORQUE-BASED QC ARCHITECTURE

In this work, three-qubit QFT for the modeling of $n$-qubit spin-torque-based QC architecture as shown in Fig. 8 is considered. The architecture consists of qubits and barriers embedded in a semiconductor channel. Each qubit has two barriers ($R$-$G$) on either side. These barriers help to isolate or

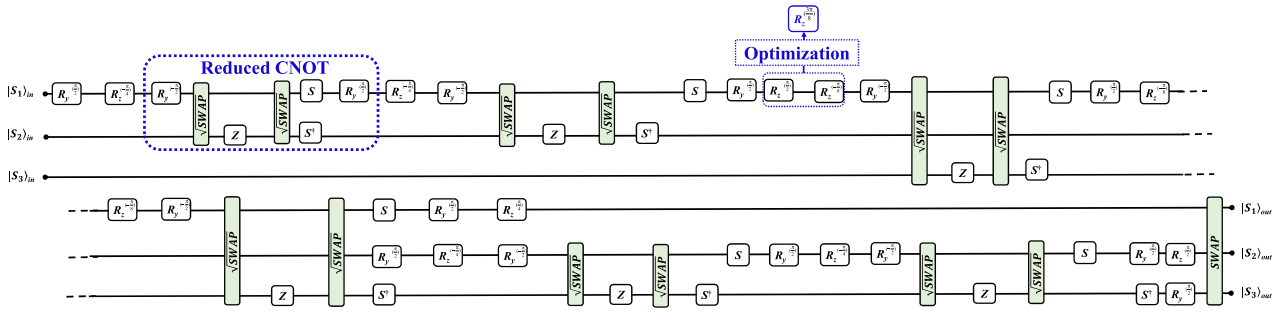


Fig. 7. Reduced/optimized decomposition of three-qubit QFT.

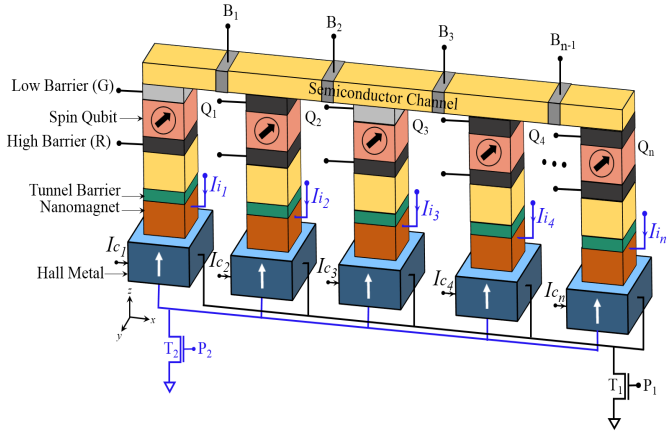


Fig. 8. Spin-torque-based $n$-qubit reconfigurable architecture.

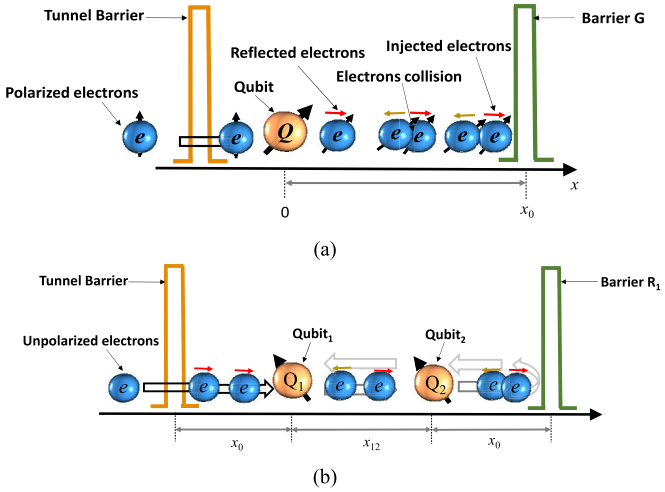


Fig. 9. (a) Electron-qubit interaction. (b) Two-qubit entanglement.

allow a qubit for the operation. The qubit operation is based on spin-torque-based interaction of the conducting electrons with qubit. For the same, the conducting electrons are required to be generated and injected into the channel. Therefore, a two-transistor assembly is provided to generate and inject the spins into the channel.

Transistors $T_1$ and $T_2$ are utilized to generate and inject the spins. The tunnel barrier (TB) is used to reduce the conductivity mismatch. The polarization of the ferromagnet decides the spin state of the injected electrons. Barriers $B_1, B_2, B_3, \ldots, B_{n-1}$ are entrenched into the channel for two-qubit entanglement operation. The distance between a qubit and barrier is $x_0$.

The single-qubit rotation and measurement in $n$-qubit architecture is as follows. The spin density matrix as expressed in the following equation represents the spin polarization of the injected electrons:

$$\rho_e = \frac{1}{2}[I + \sigma_x\hat{x} + \sigma_y\hat{y} + \sigma_z\hat{z}] \tag{17}$$

where $I$, $\sigma_x$, $\sigma_y$, and $\sigma_z$ are the unitary Pauli spin matrices.

The Hamiltonian for the interaction of injected electrons with the qubit [20] as shown in Fig. 9 is represented as

$$H = \frac{p^2}{2m^*} + J\rho_e \cdot \tilde{S}_i\delta(x) + \Gamma_{Rfl}\delta(x - x_0) \tag{18}$$

where $m*$ and $p$ are the effective mass and momentum operator of the electron, respectively, $J$ is the hyperfine or exchange interaction, $x$-$x_0$ represents the interaction distance from the reflection barrier, and $\tilde{S}_i$ is the standard basis matrix representing the $i$th qubit.

The overall spin density matrix of the $n$-qubit system is represented as

$$\rho_s = \rho_{Q_1} \otimes \rho_{Q_2} \otimes \rho_{Q_3} \ldots\ldots\ldots \otimes \rho_{Q_n} \tag{19}$$

where $\rho_s$ is overall density matrix and its order is $2^n \times 2^n$. $\rho_{Q_1}$, $\rho_{Q_2}$, $\rho_{Q_3}$, ....., and $\rho_{Q_n}$ are the individual spin density matrices of $Q_1$, $Q_2$, $Q_3$, ..., and $Q_n$, respectively.

The modified transmission coefficient matrices for singlet and triplet are derived as follows:

$$t_s^{(2)} = \frac{1}{1 + i4\Omega l - i3\Omega - 12\Omega^2 l(e^{i2kx_0} - 1)} \tag{20}$$

$$t_t^{(2)} = \frac{1}{1 + i4\Omega l + i\Omega + 4\Omega^2 l(e^{i2kx_0} - 1)} \tag{21}$$

where $\upsilon$ is the velocity of the electron, $\Omega = J/\hbar\upsilon$, and $l = (\Gamma_{Rfl}/J)$.

With the help of (20) and (21), the qubit rotation is modeled in [17] as

$$t^{(2)} = \frac{1}{(1 + i4\Omega l)I + i\tilde{S}_i\left(\Omega - \left(i4\Omega^2 l\left(e^{i2kx_0} - 1\right)\right)\right)}. \tag{22}$$

The overall reflection matrix $R_F^{(2)}$ is obtained in the following:

$$R_F^{(2)} = r^{(2)} - e^{i2kx_0}t^{(2)}\left[I_{2^{n+1}} + e^{i2kx_0}I_{2^{n+1}}R_0\right]^{-1}I_{2^{n+1}}t^{(2)} \tag{23}$$

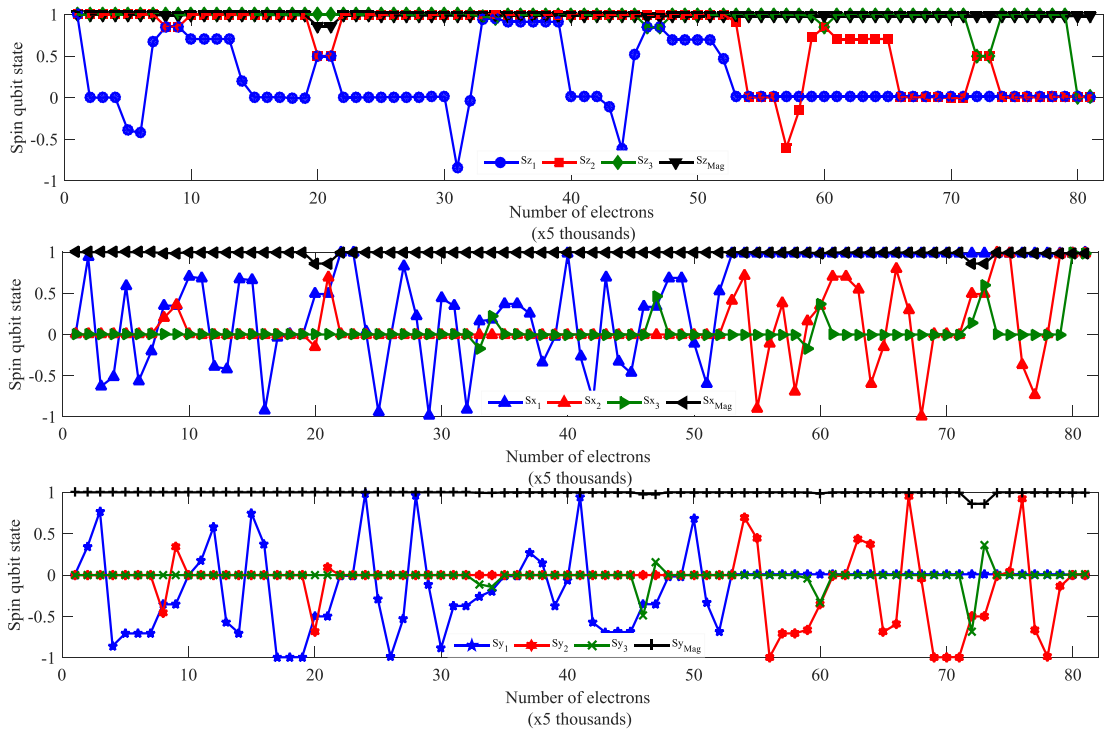


Fig. 10. Qubit-state evolution for the input |⟩ for modified (second order) transmission coefficient-based reduced/optimized decomposition of the QFT.

where $R_0$ matrix represents the reflection barrier, $I$ is the identity matrix for the $n$-qubit architecture, and $r^{(2)} = t^{(2)} - I$.

The overall fully specified density matrix is obtained as

$$\rho^{(2)} = \left[R_F^{(2)}\right]\left[\rho_e \otimes \rho_s\right]\left[R_F^{(2)\dagger}\right] \tag{24}$$

where $\rho_e$ is the spin density matrix of the moving electrons.

The single-qubit rotation is achieved through the iterative process for (24). The other aspect of the modified (second order) transmission coefficient model is the two-qubit entanglement. For the two-qubit entanglement, the barrier heights of respective $B$s are required to be lowered. The modified (second order) transmission and reflection coefficient matrix-based two-qubit entanglement through the reflection matrix representing the interaction of moving electrons at qubits $Q_1$ and $Q_2$, and the injection side barrier are modeled as follows.

The reflection matrix at $Q_1$ is

$$R_{F_1}^{(2)} = r_1^{(2)} - e^{i2kx_0} t_1^{(2)} \left[I_{2^{n+1}} + e^{i2kx_0} I_{2^{n+1}} R_0\right]^{-1} I_{2^{n+1}} t_1^{(2)}. \tag{25}$$

The reflection matrix at $Q_2$ is

$$R_{F_2}^{(2)} = r_2^{(2)} - e^{i2kx_0} t_2^{(2)} \left[I_{2^{n+1}} + e^{i2kx_0} I_{2^{n+1}} R_{F_1}^{(2)}\right]^{-1} I_{2^{n+1}} t_2^{(2)}. \tag{26}$$

The overall reflection matrix at the injection side barrier is

$$R_{F_b}^{(2)} = r_b^{(2)} - e^{i2kx_{12}} t_b^{(2)} \left[I_{2^{n+1}} + e^{i2kx_{12}} I_{2^{n+1}} R_{F_2}^{(2)}\right]^{-1} I_{2^{n+1}} t_b^{(2)}. \tag{27}$$

For the two-qubit entanglement, $R_{F_b}^{(2)}$ is used in (24) for the iterative process. At the end of the iterative process, the partial trace on $\rho^{(2)}$ provides the states of entangled qubits.

The conventional, reduced, and optimized forms of the QFT are realized on the spin-torque-based QFT. For the representation purpose, the state evolution of input state |000⟩ is shown in Fig. 10.

## VI. Performance Analysis of Three-Qubit QFT

The performance of the modified (second order) transmission coefficient-based three-qubit QFT is analyzed based on the reduction in number of electrons required, deviation in the qubit states at the output, and QFT fidelity for all possible combinations of the input states, and its ability to trace the periodicity. The number of electrons required for the QFT realization depends on the number of operations involved to perform the QFT; angle of rotation for single-qubit operations; and two-qubit entanglement. There is a considerable reduction in the number of electrons required for the reduced/optimized forms of the QFT. The magnitude and phase difference between conventional, reduced, and optimized forms of the QFT for the input |100⟩ are shown in Fig. 11. Ideally, the respective phase difference and magnitude difference should be zero. However, the magnitude difference and phase difference between the first-order conventional and modified (second order) matrix-based conventional QFTs is large in comparison with other respective magnitude and phase differences due to 34.52% more number of operations is required for the conventional decomposition; and the effect of the ratio of height of the injection side barrier to the exchange interaction on the single-qubit rotation and two-qubit entanglement.

The expression for the fidelity given in [21] for the model used in this article is

$$F = \frac{Tr(\rho_d \rho_o)}{\sqrt{Tr\left(\rho_d^2\right)}\sqrt{Tr\left(\rho_o^2\right)}} \sqrt{\frac{Tr\left(\rho_o^2\right)}{Tr\left(\rho_{\text{in}}^2\right)}} \tag{28}$$

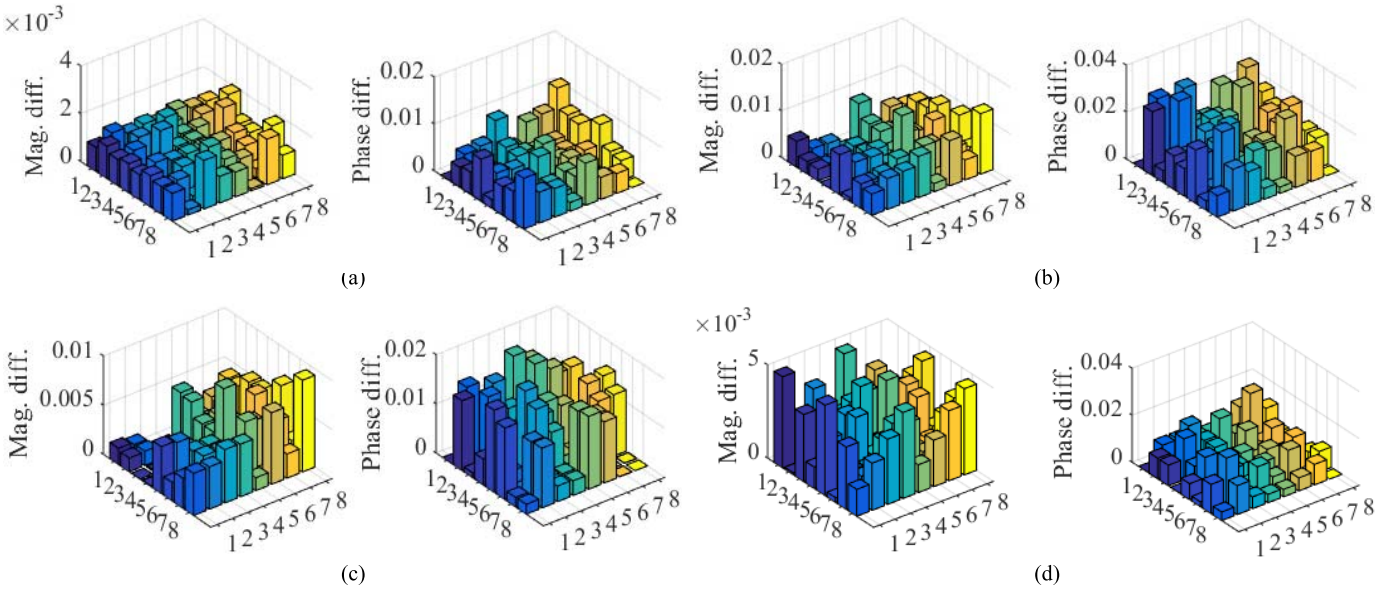


Fig. 11. Magnitude and phase difference for the input |⟩ between (a) first-order conventional and first-order reduced QFT, (b) first-order conventional and modified (second order) matrix-based conventional QFT, (c) first-order reduced and modified (second order) order reduced QFT, and (d) modified (second order) order conventional and modified (second order) order reduced QFT.

TABLE II
QFT FIDELITY FOR CONVENTIONAL AND REDUCED THREE-QUBIT QFT

| Input States | First order conventional (%) | Modified (second) order conventional (%) | First order reduced (%) | Modified (second) order reduced (%) |
|---|---|---|---|---|
| $\|000\rangle$ | 99.98 | 99.81 | 99.98 | 99.90 |
| $\|001\rangle$ | 99.91 | 99.92 | 99.99 | 99.94 |
| $\|010\rangle$ | 99.99 | 99.86 | 99.99 | 99.81 |
| $\|011\rangle$ | 99.99 | 99.92 | 99.99 | 99.94 |
| $\|100\rangle$ | 99.98 | 99.86 | 99.99 | 99.94 |
| $\|101\rangle$ | 99.97 | 99.93 | 99.99 | 99.96 |
| $\|110\rangle$ | 99.98 | 99.81 | 99.99 | 99.96 |
| $\|111\rangle$ | 99.97 | 98.82 | 99.98 | 99.77 |

where $\rho_d$, $\rho_o$, and $\rho_{\text{in}}$ are desired or ideal output states spin density matrix, obtained states spin density matrix, and input states spin density matrix. The fidelity comparison for all forms of the three-qubit QFT is given in Table II. The first-order conventional, first-order reduced, modified (second order) conventional, and modified (second order) reduced three-qubit QFTs have the average fidelities of 99.97%, 99.98%, 99.74%, and 99.90%, respectively.

The most important aspect of the QFT is periodicity extraction. An input state preparation [Fig. 12(a)] is required to extract the periodicity of the three-qubit QFT. Therefore, the input state is prepared [Fig. 12(b)] and subsequently, QFT is obtained for the input as shown in [Fig. 12(c)]. It is observed that the output density matrix is periodic with a period of four for the input of periodicity two.

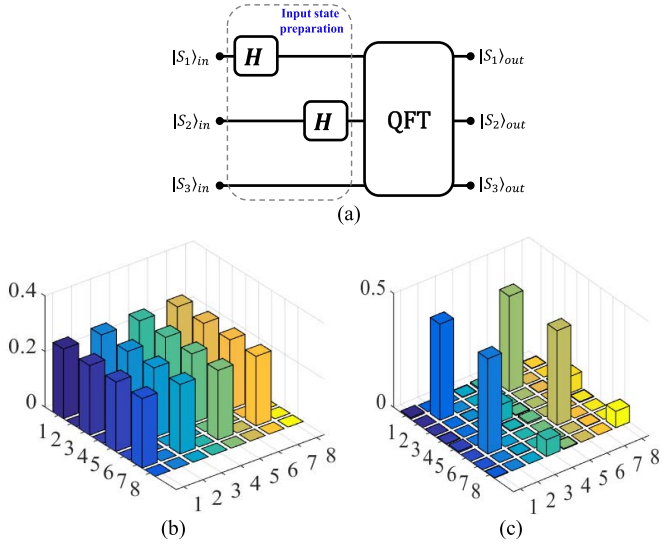


Fig. 12. QFT Periodicity estimation for the input state. (a) Quantum circuit. (b) Periodicity 2 of the input state. (c) Periodicity 4 of the output state.

TABLE III
PARAMETERS USED FOR SIMULATIONS

| Symbol | Quantity |
|---|---|
| $kx_0$ for single qubit rotation | $\pi$ |
| $kx_0$ for two-qubit entanglement | $\pi/2$ |
| $kx_{12}$ for two-qubit entanglement | $\pi$ |
| $\Omega = J/\hbar\nu$ | $\pi/16$ |
| $\Gamma_{Inj}$ for first order two-qubit entanglement | 100 |

## VII. CLIFFORD+T GATE SET-BASED QFT IMPLEMENTATION

The quantum computation needs a finite gate set to solve the problem of efficient approximation. However, there is a limitation on the basic gates sets like universal Clifford+T gate [22]. Therefore, there is need for optimized Clifford+T gate set-based quantum circuits with minimum depth [23]. In this article, an optimal-depth quantum circuit is utilized

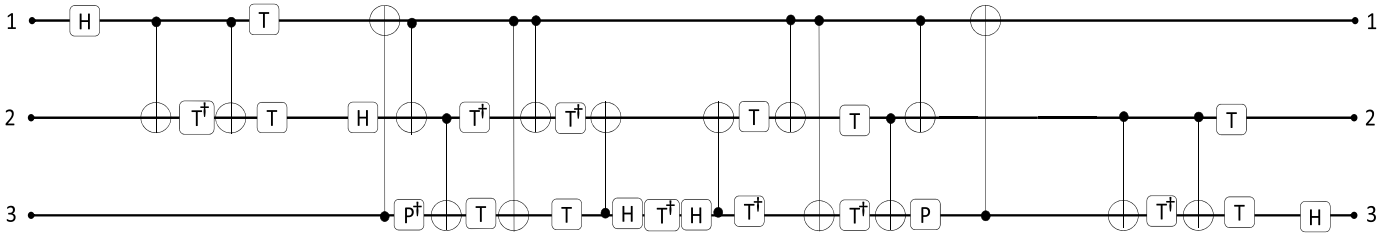

Fig. 13. Clifford+T gate set-based QFT.

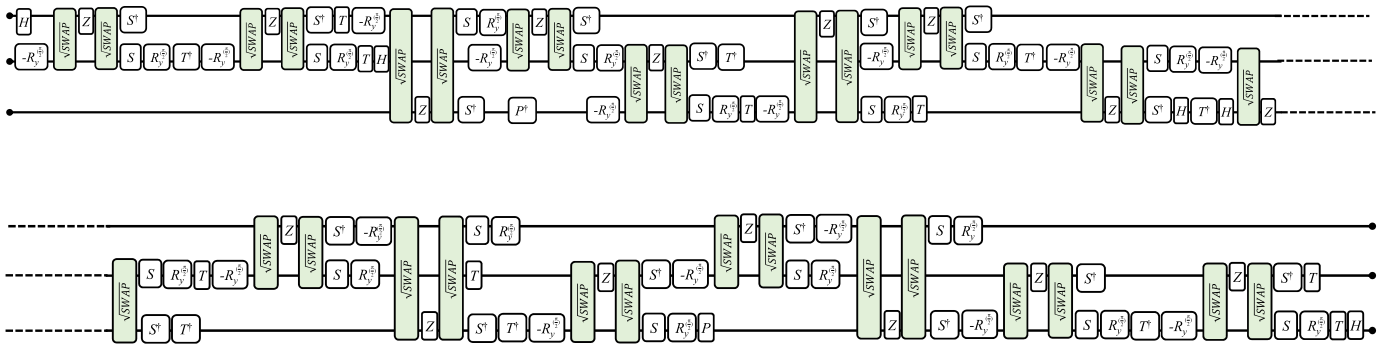

Fig. 14. Reduced decomposition of the Clifford+T gate-based QFT.

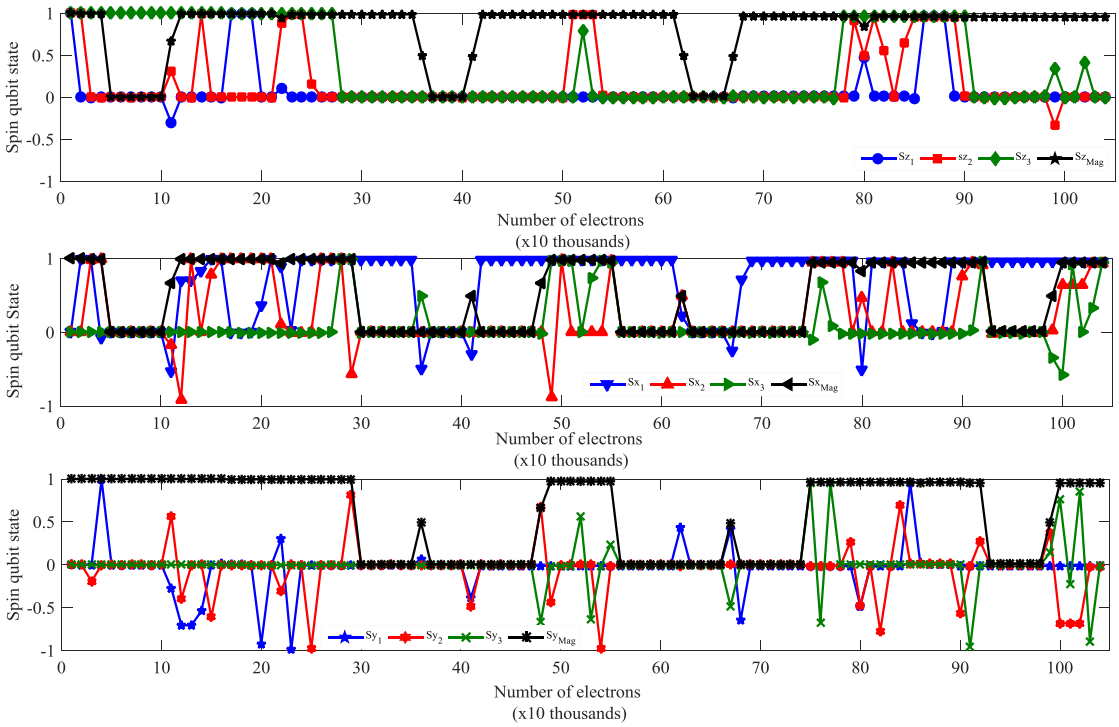


Fig. 15. Qubit state evolution of the Clifford+T gate set-based three-qubit QFT for "000" input.

to implement the Clifford+T gate-based three-qubit QFT (Fig. 12). The number of elementary gates, $T$-depth, and total depth of the quantum circuit is 40, 9, and 32, respectively. The optimal decomposition of the Clifford+T gate-based QFT is shown in Fig. 13. The state evolution of the spin-qubit state is shown in Fig. 14. It is observed from Figs. 10 and 15 that the respective input and output states are the same. Therefore, it is possible to realize the Clifford+T gate set-based QFT with the help of spin-torque-based single-qubit rotation and two-qubit entanglement model. The number of elementary operations required for the three-qubit conventional QFT and reduced QFT is 84 and 55, respectively. However, the Clifford+T gate-based QFT decomposition results in 188 elementary operations. After applying the reduction technique, it requires 134 elementary operations to realize the three-qubit QFT.

## VIII. Conclusion

In this article, QFT's optimal decomposition is achieved for the spin-torque-based QC architecture with the help of modified (second order) density matrix and optimized decomposition of the quantum circuit. Due to the optimization, there is a reduction in the number of transistor switching activities and the number of electrons required for the realization of the QFT. Moreover, the spin-torque-based QFT is able to trace the periodicity of the prepared input states of the periodicity of 4. The important outcome of the analysis is that the fidelity of the spin-torque-based three-qubit architecture is more than 99%, which encourages utilizing the spin-torque-based architecture platform for the realization of complex computing applications of which QFT is an integral part.

## Appendix

Key parameters are taken from [13] and are placed in Table III.

## References


[1] C. H. Bennett, E. Bernstein, U. V. Vazirani, and G. Brassard, "Strengths and weaknesses of quantum computing," *SIAM J. Comput.*, vol. 26, no. 5, pp. 1510–1523, Oct. 1997.

[2] E. Rieffel and W. Polak, "An introduction to quantum computing for non-physicists," *ACM Comput. Surv.*, vol. 32, no. 3, pp. 300–335, Sep. 2000.

[3] P. W. Shor, "Algorithms for quantum computation: Discrete logarithms and factoring," in *Proc. 35th Annu. Symp. Found. Comp. Sci.*, Santa Fe, NM, USA, Nov. 1994, pp. 124–134.

[4] C. M. Dawson, H. L. Haselgrove, A. P. Hines, D. Mortimer, M. A. Nielsen, and T. J. Osborne, "Quantum computing and polynomial equations over the finite field Z2," *Quantum Inf. Comput.*, vol. 5, no. 2, pp. 102–112, Mar. 2005.

[5] W. Wang, X. Jiang, L.-Z. Mu, and H. Fan, "A quantum algorithm for greatest common divisor problem," 2017, *arXiv:1707.06430*. [Online]. Available: https://arxiv.org/abs/1707.06430

[6] C. Cheng, R. Lu, A. Petzoldt, and T. Takagi, "Securing the Internet of Things in a quantum world," *IEEE Commun. Mag.*, vol. 55, no. 2, pp. 116–120, Feb. 2017.

[7] P. W. Shor, "Polynomial-time algorithms for prime factorization and discrete logarithms on a quantum computer," *SIAM J. Comput.*, vol. 26, no. 5, pp. 1484–1509, 1997.

[8] Y. S. Weinstein, M. A. Pravia, E. M. Fortunato, S. Lloyd, and D. G. Cory, "Implementation of the quantum Fourier transform," *Phy. Rev. Lett.*, vol. 86, no. 9, pp. 1889–1891, Feb. 2001.

[9] X. Tan, S. Cheng, J. Li, and Z. Feng, "Quantum key distribution protocol using quantum Fourier transform," in *Proc. IEEE 29th Int. Conf. Adv. Inf. Netw. Appl. Workshops*, Mar. 2015, pp. 96–101.

[10] D. N. Diep, "Multiparty quantum telecommunication using quantum Fourier transforms," 2017, *arXiv:1705.02608*. [Online]. Available: https://arxiv.org/abs/1705.02608

[11] L. Ruiz-Perez and J. C. Garcia-Escartin, "Quantum arithmetic with the quantum Fourier transform," *Quant. Inf. Process.*, vol. 16, no. 6, p. 152, Jun. 2017.

[12] G. Bourianoff, "The future of nanocomputing," *Computer*, vol. 36, no. 8, pp. 44–53, Aug. 2003.

[13] B. Sutton and S. Datta, "Manipulating quantum information with spin torque," *Sci. Rep.*, vol. 5, Dec. 2015, Art. no. 17912.

[14] M. Wang *et al.*, "Field-free switching of a perpendicular magnetic tunnel junction through the interplay of spin–orbit and spin-transfer torques," *Nature Electron.*, vol. 1, no. 11, pp. 582–588, Nov. 2018.

[15] M. A. Nielsen and I. L. Chuang. *Quantum Computation and Quantum Information*. Cambridge, U.K.: Cambridge Univ. Press, 2000.

[16] A. Kulkarni, S. Prajapati, and B. K. Kaushik, "Transmission coefficient matrix modeling of spin-torque-based *n*-qubit architecture," *IEEE Trans. Very Large Scale Integr. (VLSI) Syst.*, vol. 26, no. 8, pp. 1461–1470, Aug. 2018.

[17] A. Kulkarni, S. Prajapati, S. Verma, and B. K. Kaushik, "Optimal Boolean logic quantum circuit decomposition for spin-torque-based *n*-qubit architecture," *IEEE Trans. Magn.*, vol. 54, no. 10, Oct. 2018, Art. no. 4100109.

[18] C. C. Lin, A. Chakrabarti, and N. K. Jha, "Optimized quantum gate library for various physical machine descriptions," *IEEE Trans. Very Large Scale Integr. (VLSI) Syst.*, vol. 21, no. 11, pp. 2055–2068, Nov. 2013.

[19] G. Cordourier-Maruri, F. Ciccarello, Y. Omar, M. Zarcone, R. de Coss, and S. Bose, "Implementing quantum gates through scattering between a static and a flying qubit," *Phys. Rev. A, Gen. Phys.*, vol. 82, no. 5, 2010, Art. no. 052313.

[20] K. Dorai and D. Suter, "Efficient implementations of the quantum Fourier transform: An experimental perspective," *Int. J. Quantum Inf.*, vol. 3, no. 2, pp. 413–424, Jun. 2005.

[21] V. Kliuchnikov, D. Maslov, and M. Mosca, "Fast and efficient exact synthesis of single-qubit unitaries generated by clifford and T gates," *Quantum Inf. Comput.*, vol. 13, nos. 7–8, pp. 607–630, Jul. 2013.

[22] M. Amy, D. Maslov, M. Mosca, and M. Roetteler, "A meet-in-the-middle algorithm for fast synthesis of depth-optimal quantum circuits," *IEEE Trans. Comput.-Aided Design Integr. Circuits Syst.*, vol. 32, no. 6, pp. 818–830, Jun. 2013.



**Anant Kulkarni** (S'15) is currently pursuing the Ph.D. degree with the Electronics and Communication Engineering Department, IIT Roorkee, Roorkee, India.

His research interests include spintronics-based devices, circuits, and computing.

**Brajesh Kumar Kaushik** (SM'13) received the Ph.D. degree from IIT Roorkee, Roorkee, India, in 2007.

He joined the Department of Electronics and Communication Engineering, IIT Roorkee, as an Assistant Professor in 2009, where he has been an Associate Professor since 2004. His current research interests include the areas of high-speed interconnects, low-power VLSI design, memory design, carbon nanotube-based designs, organic electronics, FinFET device circuit co-design, electronic design automation (EDA), spintronics-based devices, circuits and computing, image processing, and optics- and photonics-based devices.

Dr. Kaushik is a member of many expert committees constituted by government and non-government organizations. He received many awards and recognition from the International Biographical Center (IBC), Cambridge. He has served as a General Chair, a Technical Chair, and a Keynote Speaker of many reputed international and national conferences. He is an Editor of the IEEE Transactions on Electron Devices; an Associate Editor of the *IET Circuits, Devices & Systems*; an Editor of the *Microelectronics Journal*, Elsevier; and an Editorial Board Member of the *Journal of Engineering, Design and Technology*, Emerald and *Circuit World*, Emerald. His name has been listed in Marquis Who's Who in Science and Engineering and Marquis Who's Who in the World. He has been conferred with Distinguished Lecturer (DL) Award of the IEEE Electron Devices Society (EDS) to offer EDS Chapters with quality lectures in his research domain. He also serves as an Visiting Lecturer of the SPIE society to deliver lectures in the area of spintronics and optics. He has 12 books to his credit published by reputed publishers such as CRC Press, Springer, Artech, and Elsevier. One his authored books titled "*Nanoscale Devices: Physics, Modeling, and Their Application,*" CRC Press has won 2018 Outstanding Book and Digital Product Awards in the Reference/Monograph Category from the Taylor and Francis Group.